In Situ X-ray Spectroscopy of the Electrochemical Development of Iridium Nanoparticles in Confined Electrolyte
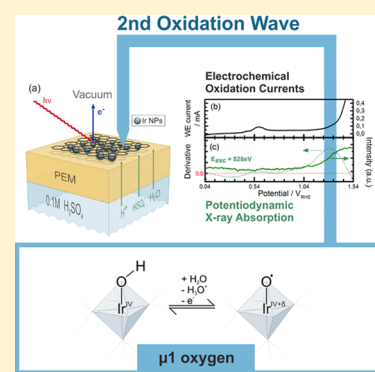
Lorenz J. Frevel,[†][iD] Rik Mom,[†][iD] Juan-Jesús Velasco-Vélez,[†][iD] Milivoj Plodinec,[†,‡] Axel Knop-Gericke,[†] Robert Schlögl,[†] and Travis E. Jones*,[†][iD]

[†]Fritz-Haber-Institut der Max-Planck-Gesellschaft, Department of Inorganic Chemistry, Faradayweg 4-6, 14195 Berlin, Germany
[‡]Rudjer Boskovic Institute, Bijenička cesta 54, 10000 Zagreb, Croatia

[S] *Supporting Information*

ABSTRACT: Iridium oxide-based catalysts are uniquely active and stable in the oxygen evolution reaction. Theoretical work attributes their activity to oxyl or μ_1-O species. Verifying this intermediate experimentally has, however, been challenging. In the present study, these challenges were overcome by combining theory with new experimental strategies. Ab initio molecular dynamics of the solid−liquid interface were used to predict spectroscopic features, whereas sample architecture, developed for surface-sensitive X-ray spectroscopy of electrocatalysts in confined liquid, was used to search for these species under realistic conditions. Through this approach, we have identified μ_1-O species during oxygen evolution. Potentiodynamic X-ray absorption additionally shows that these μ_1-O species are created by electrochemical oxidation currents in a deprotonation reaction.

INTRODUCTION

The energy sector currently lacks an affordable infrastructure for the transition from fossil fuels to zero-emission technologies. One promising building block is hydrogen.[1,2] Hydrogen can be integrated into the existing gas grid by insertion, converted into electricity via fuel cells, and used to synthesize fuels, methanol and ammonia, for example. The insufficient green production of hydrogen, however, is a bottleneck in the development of a sustainable hydrogen network.

Electrolytic water splitting in acidic electrolytes addresses this problem by making use of the intermittent nature of renewable energies to produce hydrogen at high pressures. The limiting process is the anodic oxygen evolution reaction (OER), which is plagued by high overpotentials and electrode degradation.[3] A prevalent anode material is iridium oxide, which has long been known to provide a good balance between two antagonists of an OER catalyst: activity and stability.[4,5] However, iridium is scarce and expensive, which limits its use. Large-scale production of hydrogen at affordable costs requires new catalyst materials or reduced iridium loadings.

To avoid black-box improvement strategies and enable rational design of OER catalysts, a deeper understanding of the catalysts' electronic structure during operation is necessary. We contribute to this understanding by presenting an in situ study on the chemical state of anodized iridium nanoparticles. In this study, we use predictions from ab initio molecular dynamic calculations to connect two main oxidation waves, which are well known from electrochemical studies on bulk iridium

electrodes,[6] with the formation of electron-deficient oxygen species on the catalyst surface.

In an effort to be sensitive to the active surface and the atom type, we turned to soft X-ray spectroscopy. Using low-energy photons as a probe, however, requires innovative design of the ambient pressure X-ray photoelectron spectroscopy (XPS) setup and the in situ measurement cell,[7−9] as well as the sample architecture. Previous in situ studies of this sort were carried out on proton exchange membranes (PEMs).[10−12] In one study, $Ir^{IV}O_2$ nanoparticles (NPs) were oxidized electrochemically and the authors found an Ir 4f feature with binding energy (BE) above that of the initial material.[10] The authors of another study were able to find an oxygen absorption pre-edge resonance at 529 eV via electrochemical oxidation of metallic Ir NPs.[11] They assigned this spectroscopic feature to an electron-deficient oxygen species, which is also active in CO oxidation.[13,14] In a third study, the authors oxidized metallic iridium nanoparticles in situ and found a conversion of Ir^{III} to Ir^{IV} with increasing anodic potentials.[12]

The three in situ studies mentioned above used thin layers of NPs on a PEM open to vacuum. In such a setup, water diffuses through the permeable membrane and subsequently evaporates or forms ice, which then sublimes into the vacuum. Under these conditions, a steady liquid layer is unlikely to form, which limits proton transport and thus slows down electrochemical reactions.
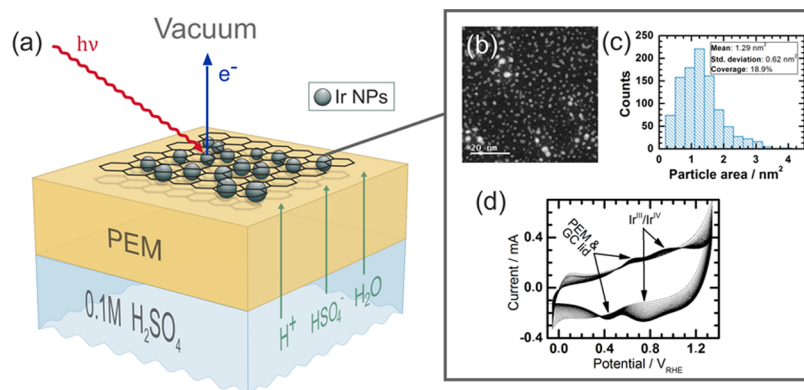
Figure 1. Experimental setup and properties: (a) Scheme of the sample architecture: a proton exchange membrane (PEM), wetted with electrolyte from the bottom, covered with nanoparticles, and sealed with graphene on the top side; (b) high-angle annular dark field micrograph of the iridium nanoparticles on a transmission electron microscopy (TEM) grid; (c) histogram of their size distribution; and (d) activation step: oxidative cycles (no. 2−50) at 500 mV/s.

■ RESULTS AND DISCUSSION

To assure proper wetting, we improved the concept of the in situ cell in ref 11 by changing the sample architecture. The membrane (or solid electrolyte) we used is permeable to all molecules essential to an electrolyte: water, anions, and protons. The catalyst nanoparticles are in direct contact with this solid electrolyte, assuring the best possible ion transport. On top of that, graphene covers the assembly of the membrane and the particle (Figure 1a). Graphene fulfills three functions: First, it is an evaporation barrier. In this function, it promotes condensation between the membrane and graphene. As soon as liquid forms, graphene is an effective barrier between liquid and vacuum.[15−17] Second, the graphene cover serves as an electrical contact for the catalyst particles, even if they are separated from each other. Third, graphene is almost transparent to photoelectrons. With such a sample preparation, the catalyst nanoparticles are in proximity to the solid electrolyte, surrounded by confined liquid, and can be accessed with soft X-ray photoelectron spectroscopy, presenting an ideal situation for in situ studies on the electronic structure of electrocatalysts.

An assembly identical to the one shown in Figure 1a but without nanoparticles was used to demonstrate condensation between the membrane and graphene. Figure 2 shows oxygen K-edges of the membrane in the dry state and in a state in which it has been wetted from the backside with 0.1 M H_2SO_4. A difference between the two spectra shows the characteristic shape of liquid water with a pre-edge feature at 535 eV, a main-

edge resonance shortly above 537 eV, and a post-edge feature at 541 eV.[17−19] Such a fingerprint is a good indicator for a densely hydrogen-bonded system, similar to liquid water. The relatively small deviation in the electronic structure of confined and bulk liquids was predicted by density functional theory (DFT) simulations of confined water between graphene sheets, where confined water was shown to adopt the electronic properties of bulk water already 0.5 nm beyond the interface to graphene.[20]

For the in situ investigation, sputtered Ir NPs were embedded in the confined electrolyte described above (Figure 1a, also compare the Experimental Section and SI, Section 1, for more details on sample preparation). High-resolution transmission electron microscopy of the NPs on a TEM grid (Figure 1b) reveals that the NPs have a mean area of 1.29 nm^2 and cover roughly a fifth of the total area (Figure 1c).

The electrode assembly was initially activated with cyclic voltammetry performed at 500 mV/s between 0.04 V with respect to the reversible hydrogen electrode (V_{RHE}) and 1.34 V_{RHE} (Figure 1d). Two oxidation waves persisted throughout the cycling: a feature at ∼0.7 V_{RHE}, originating from the membrane and the glassy carbon lid (compare Figure S5), and another at ∼1.0 V_{RHE}, which is characteristic for iridium oxides and is usually assigned to the Ir^{III}−Ir^{IV} transition.[21−24] In the following discussion, we refer to the transition at ∼1.0 V_{RHE} as the first oxidation wave. After 20 cycles, the shape of the cyclovoltagramm below 0.3 V_{RHE} narrowed and remained unchanged upon further cycling. A similar behavior has been seen before, and it has been attributed to capacitive effects on a metal−electrolyte interface below the insulating surface oxide.[6] It can be concluded that the system responds rapidly to the changing potential without signs of transport problems. The working electrode appears to form an anodic film quickly. This film is likely to be hydrated and possibly contains oxide-, oxohydroxide-, and hydroxide structures. For simplicity, we will refer to such oxidized iridium structures as iridium (hydr-)oxides.

In situ XPS confirms the hypothesis of an oxidized and hydrated shell around the iridium particles. The normalized Ir 4f XP spectrum (Figure 3a) of the fresh sample at open circuit potential (OCP) shows a main (Ir $4f_{7/2}$) BE close to the reference BE of metallic iridium. We refer to the Supporting Information (SI) for details on energy calibration. After the cyclovoltammetric activation (as described above), the
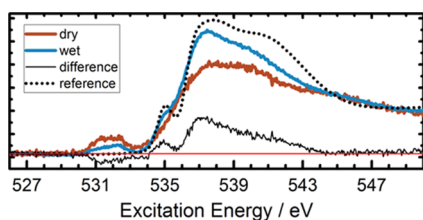

Figure 2. Wetting experiment: graphene on a proton exchange membrane (FAD55) facing vacuum; oxygen K-edge spectra, normalized at 550 eV, of a dry sample (red) and a sample that was wetted from the backside with 0.1 M H_2SO_4 (blue); the difference of both (black) and the reference spectrum (dotted) of liquid water (data from ref 18) are compared.
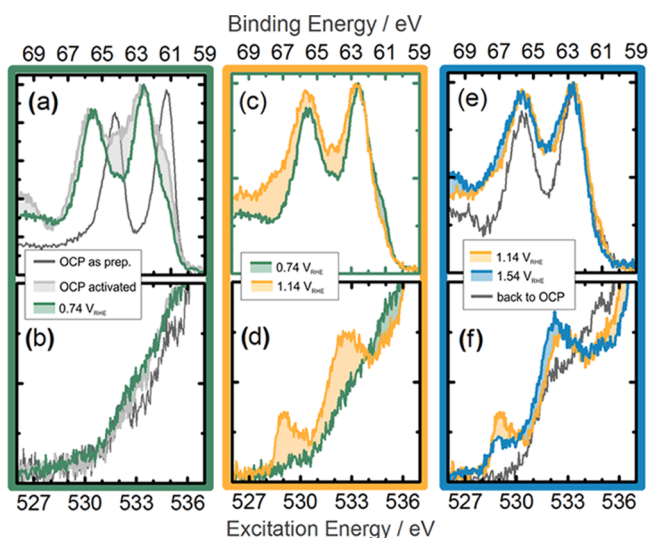
Figure 3. Potential steps: Ir 4f (top row, E_{exc} = 598 eV) and O K-edge spectra in partial electron yield (bottom row, E_{kin} = 385 eV) of iridium nanoparticles between a permeable membrane (FAD55) and graphene, equilibrated at different potential steps.

intensity of the metallic peak in the Ir 4f spectrum decreases markedly, although some amount of intensity persists. The main components in the spectrum are located above 62 eV, indicating a surface layer containing oxidized iridium. Similar BE shifts have previously been found ex situ on activated iridium electrodes[23,25] and in situ on iridium nanoparticles.[12] The spectroscopic feature at a BE of 69 eV belongs to Br 3d$_{5/2}$, since Br is a part of the permeable membrane. The respective O K-edge spectra after activation exhibit a slight increase between 532 and 534 eV (Figure 3b). More important, however, is the absence of white lines below 531 eV, which typically appear in weakly or nonhydrated iridium oxides.[13] These missing oxide absorption features and the decreasing metal contribution in the Ir 4f spectrum point toward a core−shell structure with metal in the core and a well-hydrated iridium hydroxide shell after activation. This concurs with the interpretation of previous studies on anodic films of bulk metal electrodes.[6,22−26]

Equilibration at 0.74 V$_{RHE}$ further decreases the metal contribution in the Ir 4f spectrum, which leads to a sharper and relatively symmetric peak shape (Figure 3a). The Ir 4f main-peak BE and O K-edge spectrum (Figure 3b) remain unchanged, which allows us to conclude that the hydrated iridium hydroxide formed during activation is still stable at 0.74 V$_{RHE}$. Binding energy shifts caused by the applied potential are excluded by grounding the working electrode to the electron analyzer. The small changes in electronic structure at 0.74 V$_{RHE}$, compared with that at OCP, can be explained by the low conductance of anodic films on iridium below 0.74 V$_{RHE}$, which was demonstrated for anodic films on bulk iridium electrodes.[26] These observations fit our spectroscopic findings well, since the shape of the Ir 4f spectrum after activation (Figure 3a) is relatively symmetric in comparison to the initial state, indicating poor conductivity or a lack of metallic screening. The dominant oxidation state of iridium before the first oxidation wave is generally believed to be +III.[6,21−24,26] The Ir^{III} 4f$_{7/2}$ contribution of such gapped iridium (hydr-)oxides is expected to appear above 62 eV, as measurements on IrOOH have shown.[27] The Ir 4f BE found

herein (Figure 3a) matches the one reported for IrOOH[27] and an Ir^{III} contribution obtained from deconvolution of in situ results.[12]

The step to 1.14 V$_{RHE}$ passes the first oxidation wave at around 1.0 V$_{RHE}$, which is generally assigned to the Ir^{III}−Ir^{IV} transition. Indeed, the electronic structure changes drastically. On the side of XPS, the Ir 4f peak position (Figure 3c) changes only marginally toward higher BEs, but a distinct feature, roughly 2 eV above the main line, appears. Such a strong high-BE feature was not resolved in the previous in situ studies mentioned above and points toward improved electrochemical conditions. The large shift would be consistent with a higher oxidation state of iridium. However, final state effects are known to play a role for iridates[28,29] and make it challenging to extract the oxidation state from Ir 4f spectra alone.

Fortunately, valence states of iridium and oxygen are strongly hybridized,[30−32] which enables the study of the electronic structure in iridium (hydr-)oxides via oxygen states. The O K-edge spectrum has proven to be particularly informative for iridium oxides, because of its distinct pre-edge features.[11,13] Three general types of oxygen species are expected on iridium (hydr-)oxide surfaces: the μ_1, μ_2, and μ_3 oxygen species, which are bound to one (μ_1), two (μ_2), or three (μ_3) iridium atoms. The (110) surface of rutile-type IrO$_2$ contains all three types and was used herein to calculate the absorption characteristics of each individual species (Figure 4).
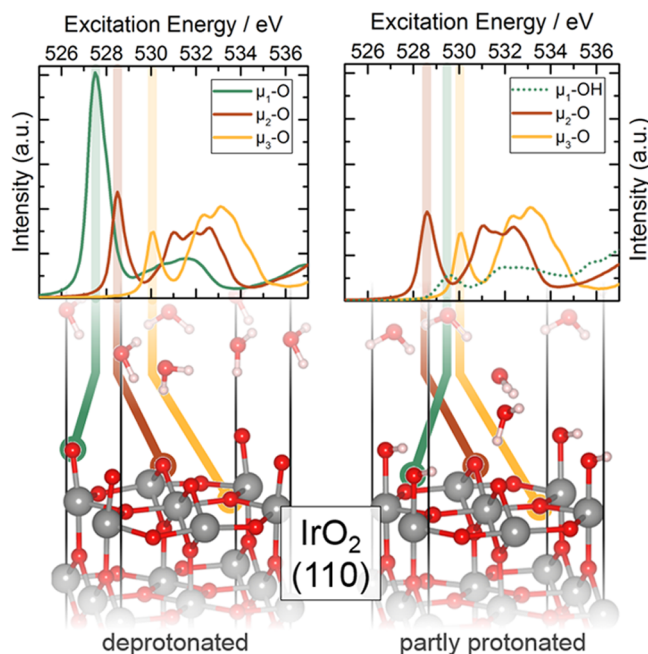

Figure 4. Molecular dynamic snapshots: Exemplary snapshots of the IrO$_2$(110) surface covered with water in a deprotonated and partially protonated version from ab initio molecular dynamics; the spectra above are averaged over four snapshots each and over all equivalent oxygen species in the given cell.

To account for influences of hydrogen bonding in a wetted environment, we performed molecular dynamics at the DFT level. In these calculations, the IrO$_2$(110) surfaces are covered with water and equilibrated at 300 K. Snapshots of the molecular dynamic simulations were then used to compute absorption spectra of each oxygen species in that snapshot. The spectra generated for each snapshot were then averaged by

type to obtain a realistic picture of their contribution to the measured spectra (details of the computational procedure are provided below and in the Supporting Information in greater detail). The results are shown in Figure 4. The absorption of all three types of oxygen, namely, μ_1, μ_2, and μ_3, exhibit similar characteristics: a pre-edge feature, due to transitions from O 1s to O 2p hybridized with Ir π^*-like states and a broader band ~3 eV above the pre-edge feature, due to transitions from O 1s to O 2p hybridized with Ir σ^*-like states. The energy shift of the pre-edge feature calibrated to the white line of bulk IrO$_2$, however, is distinct for the three types of oxygen species: the pre-edge of the μ_1-O species appears at ~528 eV, the one of μ_2-O at ~529 eV, and the one of μ_3-O at ~530 eV, where the magnitude of the resonance's red shift is proportional to the electron deficiency of the oxygen, with the μ_1-O species showing a significant radical character (see also Supporting Information). A blue shift of the spectroscopic features was found for the protonated forms, as the spectrum for μ_1-OH with a pre-edge above 529 eV demonstrates. The magnitude of this shift, however, is influenced by hydrogen bonding (see Figure S8 and the corresponding discussion in the Supporting Information). With these trends identified, it becomes possible to understand the absorption experiments.

Figure 3d shows the O K-edge spectra before and after the first oxidation wave, at 0.74 and 1.14 V$_{RHE}$, respectively. The change is drastic: absorption features at 529, 530, and around 533 eV appear. On the basis of the calculations discussed above, the pre-edge feature at 529 eV would be caused by μ_1-OH or μ_2-O type oxygen and the one at 530 eV by μ_3-O. The μ_1 and μ_2 types are, however, of special interest, because their deprotonated forms have been reported to be electron-deficient and prone to form the oxygen−oxygen bond in a peroxo-mechanism.[11,33] Interestingly, the relatively strong feature at 529 eV in Figure 3d appears after the first oxidation wave, well below the onset of the OER. Oxygen species absorbing at 529 eV can therefore be created in the first oxidation wave and appear to be stable at 1.14 V$_{RHE}$.

In the step from 1.14 to 1.54 V$_{RHE}$, the second oxidation wave is crossed. The assignment of this oxidation wave to a certain transition is still under discussion. The (further) oxidation of iridium from +IV to +V[23,24,34] and the oxidation of oxygen from −II to −I[11] have been suggested. The two explanations differ in their predictions where additional holes tend to localize in a zero-order approximation (covalent bonding between oxygen and iridium leads to sharing of the hole character[31,32]). The recorded Ir 4f spectrum in the OER, at 1.54 V$_{RHE}$, (Figure 3e) is slightly broadened on the high-BE side and shows a reduced metal contribution, suggesting that the sample is indeed oxidized further. The O K-edge absorption spectrum (Figure 3f) shows a reduced pre-edge feature at 529 eV and a shift of the absorption at 533 eV to lower excitation energies by almost 1 eV. The latter is likely caused by oxygen species in graphene or the membrane (compare Figure S6). Of greater interest here is the loss of intensity at 529 eV, since it is caused by the μ_1-OH and μ_2-O species. The intensity loss could be caused by multiple processes: deprotonation of the μ_1-OH species, consumption of the μ_2-O species, or condensation of the material via dehydration, which would increase the average coordination toward μ_3-O with a white line at 530 eV (compare Figure 4). However, the intensity loss could also be caused by normalization: the O K-edge spectra in Figure 3 are normalized to the edge jump at 550 eV and thus show the

intensity relative to all oxygen species, including the ones originating from graphene, the membrane, the electrolyte, and so on. Consequently, if the total number of all oxygen species changes, the relative intensity at 529 eV will also change.

To obtain more detailed information about how the iridium-related oxygen species develop with applied potential, we used potentiodynamic X-ray absorption spectroscopy. In this experiment, we track an absorption feature in an electrochemical cycle between 0.04 and 1.54 V$_{RHE}$. Potentiodynamic X-ray absorption has several advantages over the steady-state experiment described above. First, the absorption intensity is relative to the intensity of the starting point at 0.04 V$_{RHE}$ and the pre-edge region is therefore independent of the total amount of oxygen. Second, the development of the spectroscopic features can be directly related to electrochemical currents, since both are recorded simultaneously and are related to charge.

The spectroscopic results for voltammetric cycles at 25 mV/ s are summarized in Figure 5, and a reference measurement
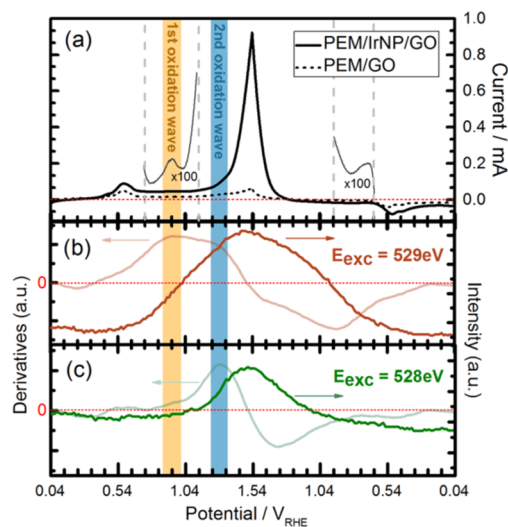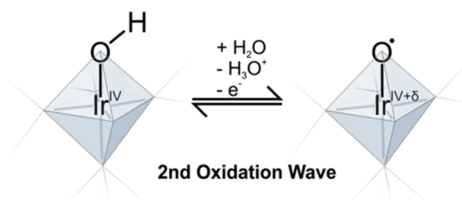

Figure 5. Potentiodynamic X-ray absorption: (a) current of the working electrode, consisting of a PEM with iridium nanoparticles and covered with graphene, over the turn of an electrochemical cycle between 0.04 and 1.54 V$_{RHE}$ at 25 mV/s; the current of a comparable sample without catalyst is shown as a dotted line; (b) and (c) show the total electron yield (red and green) at excitation energies of 529 and 528 eV, respectively; the smoothened time derivatives are shown in light red and light green.

without iridium nanoparticles is provided for comparison in the Supporting Information (Figure S7). The currents of the working electrode are given in Figure 5a for the sample and the blank as a solid or dotted line, respectively. The normalized absorption (normalization procedure in SI, Section 3) at 529 eV has its onset at roughly 0.74 V$_{RHE}$ (Figure 5b), which aligns well with the onset of the first oxidation wave. In the time derivative of the same absorption signal (compare SI, Section 3), this appears even clearer: the maximal increase of the absorption at 529 eV coincides with the current maximum of the first oxidation wave. Hence, the formation of the μ_1-OH and μ_2-O oxygen species, which absorb at 529 eV, is coupled with an electron transfer, giving rise to the first oxidation wave. Thereafter, the absorption signal continues to increase and falls with decreasing potentials. A consumption process of the oxygen species absorbing at 529 eV is not directly evident from

the intensity in the potentiodynamic absorption experiment. However, the time derivative of the tracked intensity gives the first indication of consumption: growth of the absorption at 529 eV slows down after passing the first oxidation wave and decelerates swiftly while passing the second oxidation wave. It stands to reason that deprotonation of the μ_1-OH species (Scheme 1) causes this swift change.

Scheme 1. Structural Drawing: Deprotonation and Oxidation of a μ_1-O Species, Suggested To Be Linked to the Second Oxidation Wave at ~1.4 V_{RHE}

We tested the μ_1 deprotonation hypothesis by tracking the absorption of the intense pre-edge feature predicted for μ_1-O (Figure 4) over time and changing potentials. Positively, absorption at 528 eV starts with the onset of the second oxidation wave, reaches its maximum, and quickly decays in the reverse scan (Figure 5c). The respective derivative also shows clearly that the maximum gain in the absorption signal at 528 eV slows down the growth of the absorption intensity at 529 eV. These findings support the deprotonation hypothesis suggested above. It appears that μ_1-OH, with a small contribution to the absorption at 529 eV, is transformed into μ_1-O with a sharp pre-edge absorption at ~528 eV during the second oxidation wave. Consistently, the white lines of O K-edges at constant potential broaden toward low excitation energies (Supporting Information, Figures S2 and S4).

Further support for the deprotonation hypothesis comes from the theoretical calculation of the deprotonation potential. The deprotonation step from μ_1-OH to μ_1-O was calculated to be ~1.5 V_{NHE} (see the Supporting Information for more details), which is in fair agreement with the experimental value. Creation of a μ_1-O species at the onset of the OER also explains the shortening of the Ir−O bond length at high potentials observed in many EXAFS studies:[24,31,34−37] the average equilibrium bond length of μ_1-O(H) in our ab initio molecular dynamics calculations decreases from 1.98 to 1.81 Å when deprotonating μ_1-OH to μ_1-O.

As we have seen, many pieces of evidence suggest that a μ_1-O species is created by deprotonation at the onset of the OER, where a second oxidation wave is expected.[6,11,22] The electron-deficient nature of the μ_1-O species makes them susceptible to the attack by water in the O−O bond formation step. In fact, DFT calculations performed at constant potential suggest that such μ_1-O species with unpaired spins are the active sites for O−O bond formation during OER.[38]

On a final note, the absorption features below 530 eV (Figure 3f) and the high-BE shoulder 2 eV above the Ir 4f main line (Figure 3e) almost completely disappear after a few minutes at OCP. This demonstrates general reversibility and proper electrochemical response of the investigated system and underlines that the spectroscopic features discussed herein are relevant to the electrochemical cycle of iridium (hydr-)oxides in the oxygen evolution reaction.

CONCLUSION

We suggest a sample architecture allowing for surface-sensitive X-ray spectroscopy under confined liquid, and we studied the electrochemical oxidation of iridium nanoparticles using this technique. We found experimental evidence of a connection between the first two oxidation waves (around 1.0 and 1.4 V_{RHE}) and two absorption features. We assigned these features to two classes of oxygen species (μ_2-O and μ_1-O, respectively) on the basis of ab initio molecular dynamics calculations coupled with the solution of the Bethe−Salpeter equation for the O K-edges. Both oxygen species appear to be electron-deficient in the calculations and are possible candidates for the oxygen−oxygen bond formation. However, μ_1-O was predicted to be the more active of these two oxygen species.[38] Potentiodynamic X-ray absorption provides evidence that μ_1-O is created at the onset of the OER via a deprotonation mechanism.

EXPERIMENTAL AND COMPUTATIONAL METHODS

As a proton exchange membrane, we used fumatech's FAD55 membrane, which is permeable to water, protons, and anions. Iridium nanoparticles were sputter-deposited onto a disk of the same membrane in an argon atmosphere. The graphene blanket swimming on a liquid solution was captured with the membrane assembly from below and dried afterward. The samples were stored in sodium sulfate solution until their use in the in situ cell setup.

The sample assemblies described above were mounted onto the in situ cell described earlier[11] and used in a near-ambient pressure X-ray spectroscopy setup connected to the ISISS beamline at the BESSY II synchrotron facility. In the rear of the sample, in the bulk electrolyte, we used an Ag/AgCl (KCl saturated) reference electrode and a platinum wire as the counterelectrode in a constant flow of 0.1 M H_2SO_4. The working electrode contact was fixed with a glassy carbon lid and grounded to the electron analyzer. The water backpressure in the experiment chamber ranged from 0.05 to 0.15 mbar.

DFT calculations were performed using the Quantum ESPRESSO package[39] and the Perdew−Burke−Ernzerhof[40] exchange and correlation potential. For calculations of the absorption spectra, we treated the electron−hole problem with the Bethe−Salpeter equation[41] within many-body perturbation theory. All calculations were performed as non-spin-polarized with the inclusion of scalar relativistic effects.

A more detailed description of the experimental and computational procedure can be found in the Supporting Information.

ASSOCIATED CONTENT

ⓢ Supporting Information

The Supporting Information is available free of charge on the ACS Publications website at DOI: 10.1021/acs.jpcc.9b00731.

> Detailed experimental procedure (sample preparation, transmission electron microscopy, the in situ measurements, and spectroscopic analysis), supplement to the in situ experiments with Ir nanoparticles, blank measurements without catalyst, supporting evidence, and computational details. (PDF)

AUTHOR INFORMATION

Corresponding Author

*E-mail: trjones@fhi-berlin.mpg.de. Tel: +49 30 8413 4421.

ORCID

Lorenz J. Frevel: 0000-0002-2622-5166

Rik Mom: 0000-0002-5111-5591

Juan-Jesús Velasco-Vélez: 0000-0002-6595-0168

Travis E. Jones: 0000-0001-8921-7641

Notes

The authors declare no competing financial interest.

REFERENCES

(1) Schlögl, R. Sustainable Energy Systems: The Strategic Role of Chemical Energy Conversion. *Top. Catal.* **2016**, *59*, 772−786.

(2) Sartbaeva, A.; Kuznetsov, V. L.; Wells, S. A.; Edwards, P. P. Hydrogen Nexus in a Sustainable Energy Future. *Energy Environ. Sci.* **2008**, *1*, 79−85.

(3) Carmo, M.; Fritz, D. L.; Mergel, J.; Stolten, D. A Comprehensive Review on PEM Water Electrolysis. *Int. J. Hydrogen Energy* **2013**, *38*, 4901−4934.

(4) Trasatti, S. Electrocatalysis in the Anodic Evolution of Oxygen and Chlorine. *Electrochim. Acta* **1984**, *29*, 1503−1512.

(5) Miles, M. H.; Thomason, M. A. Periodic Variations of Overvoltages for Water Electrolysis in Acid Solutions from Cyclic Voltammetric Studies. *J. Electrochem. Soc.* **1976**, *123*, 1459−1461.

(6) Conway, B. E.; Mozota, J. Surface and Bulk Processes at Oxidized Iridium Electrodes-II. Conductivity-Switched Behaviour of Thick Oxide Films. *Electrochim. Acta* **1983**, *28*, 9−16.

(7) Axnanda, S.; Crumlin, E. J.; Mao, B.; Rani, S.; Chang, R.; Karlsson, P. G.; Edwards, M. O. M.; Lundqvist, M.; Moberg, R.; Ross, P.; et al. Using "Tender" X-Ray Ambient Pressure X-Ray Photoelectron Spectroscopy as A Direct Probe of Solid-Liquid Interface. *Sci. Rep.* **2015**, *5*, No. 9788.

(8) Itkis, D. M.; Velasco-Vélez, J. J.; Knop-Gericke, A.; Vyalikh, A.; Avdeev, M. V.; Yashina, L. V. Probing Operating Electrochemical Interfaces by Photons and Neutrons. *ChemElectroChem* **2015**, *2*, 1427−1445.

(9) Knop-Gericke, A.; Pfeifer, V.; Velasco-Velez, J.-J.; Jones, T.; Arrigo, R.; Hävecker, M.; Schlögl, R. In Situ X-Ray Photoelectron Spectroscopy of Electrochemically Active Solid-Gas and Solid-Liquid Interfaces. *J. Electron Spectrosc. Relat. Phenom.* **2017**, *221*, 10−17.

(10) Sanchez Casalongue, H. G.; Ng, M. L.; Kaya, S.; Friebel, D.; Ogasawara, H.; Nilsson, A. In Situ Observation of Surface Species on Iridium Oxide Nanoparticles during the Oxygen Evolution Reaction. *Angew. Chem., Int. Ed.* **2014**, *53*, 7169−7172.

(11) Pfeifer, V.; Jones, T. E.; Velasco Vélez, J. J.; Arrigo, R.; Piccinin, S.; Hävecker, M.; Knop-Gericke, A.; Schlögl, R. In Situ Observation of Reactive Oxygen Species Forming on Oxygen-Evolving Iridium Surfaces. *Chem. Sci.* **2017**, *8*, 2143−2149.

(12) Lettenmeier, P.; Majchel, J.; Wang, L.; Saveleva, V. A.; Zafeiratos, S.; Savinova, E. R.; Gallet, J.-J.; Bournel, F.; Gago, A. S.; Friedrich, K. A. Highly Active Nano-Sized Iridium Catalysts: Synthesis and Operando Spectroscopy in a Proton Exchange Membrane Electrolyzer. *Chem. Sci.* **2018**, *9*, 3570−3579.

(13) Pfeifer, V.; Jones, T. E.; Velasco Vélez, J. J.; Massué, C.; Arrigo, R.; Teschner, D.; Girgsdies, F.; Scherzer, M.; Greiner, M. T.; Allan, J.; et al. The Electronic Structure of Iridium and Its Oxides. *Surf. Interface Anal.* **2016**, *48*, 261−273.

(14) Pfeifer, V.; Jones, T. E.; Wrabetz, S.; Massué, C.; Velasco Vélez, J. J.; Arrigo, R.; Scherzer, M.; Piccinin, S.; Hävecker, M.; Knop-Gericke, A.; et al. Reactive Oxygen Species in Iridium-Based OER Catalysts. *Chem. Sci.* **2016**, *7*, 6791−6795.

(15) Velasco-Vélez, J. J.; Pfeifer, V.; Hävecker, M.; Weatherup, R. S.; Arrigo, R.; Chuang, C. H.; Stotz, E.; Weinberg, G.; Salmeron, M.; Schlögl, R.; et al. Photoelectron Spectroscopy at the Graphene−Liquid Interface Reveals the Electronic Structure of an Electro-deposited Cobalt/Graphene Electrocatalyst. *Angew. Chem., Int. Ed.* **2015**, *54*, 14554−14558.

(16) Nappini, S.; Matruglio, A.; Naumenko, D.; Dal Zilio, S.; Bondino, F.; Lazzarino, M.; Magnano, E. Graphene Nanobubbles on TiO2 for In-Operando Electron Spectroscopy of Liquid-Phase Chemistry. *Nanoscale* **2017**, *9*, 4456−4466.

(17) Guo, H.; Strelcov, E.; Yulaev, A.; Wang, J.; Appathurai, N.; Urquhart, S.; Vinson, J.; Sahu, S.; Zwolak, M.; Kolmakov, A. Enabling Photoemission Electron Microscopy in Liquids via Graphene-Capped Microchannel Arrays. *Nano Lett.* **2017**, *17*, 1034−1041.

(18) Nilsson, A.; Nordlund, D.; Waluyo, I.; Huang, N.; Ogasawara, H.; Kaya, S.; Bergmann, U.; Näslund, L. Å.; Öström, H.; Wernet, P.; et al. X-Ray Absorption Spectroscopy and X-Ray Raman Scattering of Water and Ice; an Experimental View. *J. Electron Spectrosc. Relat. Phenom.* **2010**, *177*, 99−129.

(19) Schreck, S.; Wernet, P. Isotope Effects in Liquid Water Probed by Transmission Mode X-Ray Absorption Spectroscopy at the Oxygen K-Edge. *J. Chem. Phys.* **2016**, *145*, No. 104502.

(20) Cicero, G.; Grossman, J. C.; Schwegler, E.; Gygi, F.; Galli, G. Water Confined in Nanotubes and between Graphene Sheets: A First Principle Study. *J. Am. Chem. Soc.* **2008**, *130*, 1871−1878.

(21) Buckley, D. N.; Burke, L. D. The Oxygen Electrode - Part 5. - Enhancement of Charge Capacity of an Iridium Surface in the Anodic Region. *J. Chem. Soc., Faraday Trans. 1* **1975**, *71*, 1447−1459.

(22) Gottesfeld, S.; Srinivasan, S. Electrochemical and Optical Studies of Thick Oxide Layers on Iridium and Their Electrocatalytic Activities for the Oxygen Evolution Reaction. *J. Electroanal. Chem. Interfacial Electrochem.* **1978**, *86*, 89−104.

(23) Kötz, R.; Neff, H.; Stucki, S. Anodic Iridium Oxide Films - XPS-Studies of Oxidation State Changes and O2 Evolution. *J. Electrochem. Soc.* **1984**, *131*, 72−77.

(24) Hüppauff, M.; Lengeler, B. Valency and Structure of Iridium in Anodic Iridium Oxide Films. *J. Electrochem. Soc.* **1993**, *140*, 598−602.

(25) Hall, H. Y.; Sherwood, P. M. A. X-Ray Photoelectron Spectroscopic Studies of the Iridium Electrode System. *J. Chem. Soc., Faraday Trans. 1* **1984**, *80*, 135−152.

(26) Glarum, S. H.; Marshall, J. H. The A-C Response of Iridium Oxide Films. *J. Electrochem. Soc.* **1980**, *127*, 1467−1474.

(27) Weber, D.; Schoop, L. M.; Wurmbrand, D.; Nuss, J.; Seibel, E. M.; Tafti, F. F.; Ji, H.; Cava, R. J.; Dinnebier, R. E.; Lotsch, B. V. Trivalent Iridium Oxides: Layered Triangular Lattice Iridate $K_{0.75}Na_{0.25}IrO_2$ and Oxyhydroxide IrOOH. *Chem. Mater.* **2017**, *29*, 8338−8345.

(28) Kawasaki, J. K.; Uchida, M.; Paik, H.; Schlom, D. G.; Shen, K. M. Evolution of Electronic Correlations across the Rutile, Perovskite, and Ruddelsden-Popper Iridates with Octahedral Connectivity. *Phys. Rev. B* **2016**, *94*, No. 121104(R).

(29) Weber, D.; Schoop, L. M.; Wurmbrand, D.; Nuss, J.; Seibel, E. M.; Tafti, F. F.; Ji, H.; Cava, R. J.; Dinnebier, R. E.; Lotsch, B. V. Trivalent Iridium Oxides: Layered Triangular Lattice Iridate $K_{0.75}Na_{0.25}IrO_2$ and Oxyhydroxide IrOOH. *Chem. Mater.* **2017**, *29*, 8338−8345.

(30) Ping, Y.; Galli, G.; Goddard, W. A. Electronic Structure of IrO2: The Role of the Metal d-Orbitals. *J. Phys. Chem. C* **2015**, *119*, 11570−11577.

(31) Nong, H. N.; Reier, T.; Oh, H.-S.; Gliech, M.; Paciok, P.; Vu, T. H. T.; Teschner, D.; Heggen, M.; Petkov, V.; Schlögl, R.; et al. A Unique Oxygen Ligand Environment Facilitates Water Oxidation in Hole-Doped IrNiOx Core−Shell Electrocatalysts. *Nat. Catal.* **2018**, *1*, 841−851.

(32) Velasco-Vélez, J. J.; Jones, T. E.; Streibel, V.; Hävecker, M.; Chuang, C.-H.; Frevel, L.; Plodinec, M.; Centeno, A.; Zurutuza, A.; Wang, R.; et al. Electrochemically Active Ir NPs on Graphene for OER in Acidic Aqueous Electrolyte Investigated by In Situ and Ex Situ Spectroscopies. *Surf. Sci.* **2019**, *681*, 1−8.

(33) Rossmeisl, J.; Qu, Z.-W.; Zhu, H.; Kroes, G.-J.; Nørskov, J. K. Electrolysis of Water on Oxide Surfaces. *J. Electroanal. Chem.* **2007**, *607*, 83−89.

(34) Minguzzi, A.; Locatelli, C.; Lugaresi, O.; Achilli, E.; Cappelletti, G.; Scavini, M.; Coduri, M.; Masala, P.; Sacchi, B.; Vertova, A.; et al. Easy Accommodation of Different Oxidation States in Iridium Oxide Nanoparticles with Different Hydration Degree as Water Oxidation Electrocatalysts. *ACS Catal.* **2015**, *5*, 5104−5115.

(35) Abbott, D. F.; Lebedev, D.; Waltar, K.; Povia, M.; Nachtegaal, M.; Fabbri, E.; Copéret, C.; Schmidt, T. J. Iridium Oxide for the Oxygen Evolution Reaction: Correlation between Particle Size, Morphology, and the Surface Hydroxo Layer from Operando XAS. *Chem. Mater.* **2016**, *28*, 6591−6604.

(36) Pauporté, T.; Aberdam, D.; Hazemann, J.-L.; Faure, R.; Durand, R. X-Ray Absorption in Relation to Valency of Iridium in Sputtered Iridium Oxide Film. *J. Electroanal. Chem.* **1999**, *465*, 88−95.

(37) Hillman, A. R.; Skopek, M. A.; Gurman, S. J. X-Ray Spectroscopy of Electrochemically Deposited Iridium Oxide Films: Detection of Multiple Sites through Structural Disorder. *Phys. Chem. Chem. Phys.* **2011**, *13*, 5252−5263.

(38) Ping, Y.; Nielsen, R. J.; Goddard, W. A. The Reaction Mechanism with Free Energy Barriers at Constant Potentials for the Oxygen Evolution Reaction at the IrO2 (110) Surface. *J. Am. Chem. Soc.* **2017**, *139*, 149−155.

(39) Giannozzi, P.; Baroni, S.; Bonini, N.; Calandra, M.; Car, R.; Cavazzoni, C.; Ceresoli, D.; Chiarotti, G. L.; Cococcioni, M.; Dabo, I.; et al. QUANTUM ESPRESSO: A Modular and Open-Source Software Project for Quantum Simulations of Materials. *J. Phys. Condens. Matter* **2009**, *21*, No. 395502.

(40) Perdew, J. P.; Burke, K.; Ernzerhof, M. Generalized Gradient Approximation Made Simple. *Phys. Rev. Lett.* **1996**, *77*, 3865−3868.

(41) Vinson, J.; Rehr, J. J.; Kas, J. J.; Shirley, E. L. Bethe-Salpeter Equation Calculations of Core Excitation Spectra. *Phys. Rev. B* **2011**, *83*, No. 115106.